Biogeosciences Discuss., 11, 12531–12569, 2014
www.biogeosciences-discuss.net/11/12531/2014/
doi:10.5194/bgd-11-12531-2014

Biogeosciences Discussions
Open Access

Dissolved greenhouse gases (nitrous oxide and methane) associated with the natural iron-fertilized Kerguelen region (KEOPS 2 cruise) in the Southern Ocean

L. Farías[1], L. Florez-Leiva[2], V. Besoain[1,3], and C. Fernández[4,5,6]

[1]Departamento de Oceanografía. Universidad of Concepción and Centro de Ciencia del Clima y la Resiliencia (CR)[2], Chile
[2]Programa de Biología, Universidad del Magdalena, Santa Marta, Colombia
[3]Escuela de Ciencias del Mar, Pontificia Universidad Católica de Valparaíso, Chile
[4]Sorbonne Universités, UPMC Univ Paris 06, UMR 7621, Laboratoire d'Océanographie Microbienne, Observatoire Océanologique, 66650 Banyuls/mer, France and Department of Oceanography and Interdisciplinary Center for Aquaculture Research (INCAR), University of Concepción, Chile
[5]CNRS, UMR 7621, Laboratoire d'Océanographie Microbienne, Observatoire Océanologique, 66650 Banyuls/mer, France
[6]Department of Oceanography, COPAS SurAustral program and Interdisciplinary center for Aquaculture Research (INCAR), University of Concepción, Chile

Received: 23 June 2014 – Accepted: 4 July 2014 – Published: 20 August 2014

Correspondence to: L. Farias (lfarias@profc.udec.cl)

Published by Copernicus Publications on behalf of the European Geosciences Union.

Abstract

The concentrations of greenhouse gases (GHGs) like nitrous oxide (N_2O) and methane (CH_4) were measured in the Kerguelen Plateau Region (KPR), an area with annual microalgal bloom caused by natural Fe fertilization, which may stimulate microbes involved in GHG cycling. This study was carried out during the KEOPS 2 cruise during the austral spring of 2011. Two transects were sampled along and across the KRP, the north–south (N–S) transect (46–51° S, 72° E meridian) and the west–east (W–E) transect (66–75° E, 48.3° S latitude), both associated with the presence of a plateau, polar fronts and other mesoscale features. The W–E transect had N_2O levels ranging from equilibrium (105 %) to light supersaturation (120 %) with respect to the atmosphere. CH_4 levels fluctuated dramatically, with intense supersaturations (120–970 %) in areas close to the coastal waters of Kerguelen Island and in the polar front (PF). There, Fe and nutrient fertilization seem to promote high total chlorophyll *a* (TChl *a*) levels. The distribution of both gases was more homogenous in the N–S transect, but CH_4 peaked at southeastern stations of the KPR (A3 stations), where phytoplankton bloom was observed. Both gases responded significantly to the patchy distribution of particulate matter as Chl *a*, stimulated by Fe supply by complex mesoscale circulation. While CH_4 appears to be produced mainly at the pycnoclines, N_2O seems to be consumed superficially. Air–sea fluxes for N_2O (from −10.5 to 8.65, mean 1.71 $\mu mol\, m^{-2}\, d^{-1}$), and for CH_4 (from 0.32 to 38.1, mean 10.07 $\mu mol\, m^{-2}\, d^{-1}$) reflected sink and source behavior for N_2O and source behavior for CH_4, with considerable variability associated with a highly fluctuating wind regime and, in the case of CH_4, due to its high superficial levels that had not been reported before in the Southern Ocean and may be caused by an intense microbial CH_4 cycling.

BGD
11, 12531–12569, 2014

1 Introduction

The increasing concentration of greenhouse gases (GHGs) like CO_2, N_2O and CH_4 in the troposphere is linked to global temperature changes. Additionally, the increasing concentration of ozone-depleting gases (such as chlorofluorocarbons and N_2O) in the stratosphere is weakening the ozone shield, allowing higher levels of damaging ultraviolet radiation to reach the Earth's surface. This means that GHGs play a major role in the Earth's radiative balance. The strength of each GHG is determined by its respective residence time in the atmosphere (Cicerone and Orelamland, 1988) and the magnitude of its emissions, in which oceans play an important role (IPCC, 2007).

Although oceans are generally considered a net source of the GHGs like N_2O and CH_4 in the atmosphere, the oceanic distribution of these GHGs and the amount exchanged by the air–sea interface is highly variable (Nevison et al., 1995; Holmes et al., 2000; Rhee et al., 2009). Thus, source and sink behaviors of GHGs have been observed on different spatial and temporal scales. In general terms, these behaviors depend on biological and physical processes that promote outgassing or sequester mechanisms like upwelling and downwelling.

Physical and biological features of the Southern Ocean suggest the potential for both the production and removal of CH_4 and N_2O (Rees et al., 1999; Tilbrok and Karl, 1994), although very little information on dissolved N_2O and CH_4 distributions in that region is currently available. Increased gas solubility in low-temperature Sub- and Antarctic waters, combined with downwelling associated with intermediate and deep water formation over the convergence band (Antarctic Polar Frontal Zone or "PFZ") or low-temperature Antarctic waters combined with the upwelling of deep and intermediate waters in the southern part of the PFZ) (Parker and Viver, 2012) could generate situations of outgassing or gas sequester. These processes could result in substantial spatial variation in gas exchanges in this region.

The Indian Ocean is the third largest in the world, covering approximately 20 % of the Earth's surface. Its southern part, defined as part of the Sub-Tropical Convergence

BGD
11, 12531–12569, 2014

(e.g., south of the Subtropical Front) and the polar front zone (PFZ), is characterized by marked biogeochemical gradients, most of which are driven by Fe availability (Law and Ling, 2001; Walter et al., 2005) as are the waters of the Kerguelen Plateau (Blain et al., 2007, 2008). N_2O sinks and/or sources can be observed occasionally in different regions of the ocean (Butler et al., 1989; Law and Ling, 2001; Charpentier et al., 2010), whereas CH_4 sources have always been found in all the world's oceans (Forster et al., 2009). Thus, this study represents one of the first contributions about gas contents in the Southern Ocean under the influence of natural annual fertilization events in the KPR.

GHG concentrations and fluxes in aquatic ecosystems depend primarily on organic matter (OM) production and oxygen levels (Codispoti et al., 2001). The latter determines whether aerobic or anaerobic processes are responsible for OM respiration (Wolfe, 1971). N_2O is formed during the first step of nitrification, the aerobic oxidation of NH_4^+ to NO_2^- and partial denitrification and the anaerobic reduction of NO_3^-/NO_2^- to N_2O. It can also be consumed by complete denitrification via dessimilatory reduction to N_2 (Codispoti and Cristiensen, 1985) or assimilatory N_2O reduction to NH_4^+ (Farias et al., 2013). CH_4, on the other hand, is mainly formed by methanogens or methylotrophs during anaerobic OM degradation (Wuebble and Hayboe, 2001) and is consumed via aerobic methanothophy (Hanson and Hanson, 1996).

Since Southern Ocean waters are well oxygenated, N_2O formed by nitrification is thought to be dominant (see Nevison et al., 2003). Possible sources of CH_4, methanogenesis in suspended particles in surface waters (Scranton and Brewer, 1977) and/or CH_4 formation derived from transformations of methyl-compounds such as methylphosphonate (MPn) cycling in the PO_4^{3-} stressed subtropical gyre (Karl et al., 2008) dimethylsulphoniopropionate (DMSP) in NO_3-depleted Arctic waters (Damm et al., 2010) and dimethilsulfate (DMS) in nutrient-rich upwelling water (Florez-Leiva et al., 2013).

The study of the role of the Southern Ocean in CH_4 and N_2O air–sea exchange can be critical to understand the factors/variables that influence GHG cycling. The KEOPS

BGD
11, 12531–12569, 2014

2 scientific program included a complete physical, biological and chemical survey of the Fe-enriched KPR that induces mesotrophic conditions, most associated with the coastal waters of Kerguelen Island, the PFZ, the southeastern part of the KPR and other mesoscale structures (Mongin et al., 2008; Lasbleiz et al., 2014); but also included Fe-depleted high-nutrient low-chlorophyll area or HNLC (west of the Kerguelen Islands, or reference station R). The study area provides a natural laboratory to explore GHG cycling and the microbial processes involved during the evolution of a phytoplankton bloom.

2 Methods

2.1 Study area

Samples were collected during the KEOPS 2 cruise at stations along the north to south or TNS (46–51° S) and across west to east or TWE (66–75° E) transects around the Kerguelen Plateau Region (Fig. 1). The cruise was on board the research vessel (RV) *Marion-Dufresne* from 11 October to 11 December 2011. Some of the sampled stations were located in the PFZ in the coastal water of Kerguelen Island (shelf) and the southeastern KPR bloom (Station A3 was studied earlier during the KEOPS 1 cruise), which are naturally Fe-enriched, while another station, St. R, located beyond the KPR and considered representative of the HNLC area off the plateau area, was sampled (Table 1). The hydrographic setting of the sampling stations was chosen according to a strategy based on real-time ocean color and altimetry satellite images (d'Ovidio et al., 2012).

2.2 Continuous and discrete sampling

Continuous vertical profiles of temperature, salinity, dissolved O_2, fluorescence and photosynthetically active radiation (PAR) were obtained using a conductivity temperature and depth (CTD) sensor. Water was sampled with a CTD-Rosette sampler (SBE 32

BGD
11, 12531–12569, 2014

24 × 10 L Carousel Water Sampler with 10 L Niskin bottles). Water samples for gases (N_2O, CH_4), nutrients and pigments (in this correlative order) were obtained at nine depths concentrated between the surface and a depth of 500 m. Water samples were taken in 20 mL glass vials for CH_4 and N_2O analyses and poisoned with $HgCl_2$ (0.1 mL of saturated $HgCl_2$ solution per vial). The vials were then sealed with butyl-rubber septums and aluminum caps, avoiding bubble formation, and stored at room temperature in darkness until laboratory analysis. Syringes of 50 mL were directly connected to the spigot of the Niskin bottles to take nutrient samples (NO_3^-, NO_2^- and PO_4^{3-} and $Si(OH)_4$) at each sampled depth. Duplicate samples were collected and drawn through a 0.45 µm Uptidisc adapted to the syringe and then immediately analyzed using an autoanalyzer (more details in Blain et al., 2014). Total chlorophyll *a* (TChl *a*) samples in triplicate were filtered into a 25 mm glass- fiber filter (GF/F), and then immediately frozen (−20 °C). Samples were kept until later analysis by high performance liquid chromatography (HPLC) (more details in Lasbleiz et al., 2014).

2.3 Chemical analysis

N_2O and CH_4 were determined by helium (He) equilibration (5 mL helium headspace and 15 mL of seawater) at 40 °C in the vial, followed by quantification via chromatography. N_2O was analyzed in a Varian 3380 Gas Chromatograph using an electron capture detector at 350 °C and connected to an autosampler device. CH_4 was analyzed in a Schimadzu 17A gas chromatograph using a flame ionization detector at 250 °C through a capillary column GS-Q at an oven temperature of 30 °C. A calibration curve was made with four concentrations for N_2O (0.1 ppm, air, 0.5 ppm, and 1 ppm by Matheson standards) for N_2O and four concentrations for CH_4 (0.5, air, 2 and 10 ppm, by Matheson standards). Both detectors linearly responded to these concentration ranges. The analytical error for the N_2O and CH_4 analyses was less than 3 % and 5 % respectively. More details regarding the analysis of both gases can be found in Farias et al. (2009). Nutrients were immediately analyzed onboard by standard automated colorimetric methods (Tréguer and LeCorre, 1975) using the continuous flow

BGD
11, 12531–12569, 2014

autoanalyser (Skalar). The precision of the method was ±50 nM, with a detection limit of 20 nM.

2.4 Data analysis

To interpret the vertical variation of N_2O and CH_4 and how biogeochemical processes may affect their concentrations, the water column was divided in two layers according to density gradient: (1) a well-mixed and (2) a subsurface from the base of the mixed layer (ML) to 500 m (arbitrary depth used only for comparison proposes). Nutrient TChl *a*, N_2O and CH_4 inventories were calculated by numerical integration of data at one meter (linear interpolation) increments based on at least 4–6 sampled depths per layer. Saturation percentages of gases were calculated from measured CH_4 and N_2O concentrations and those estimated to be in equilibrium with the current gas concentrations in the atmosphere according to NOAA register (http://www.esrl.noaa.gov/gmd/hats/combined/N2O.html), based on in situ temperature and salinity according to the solubility parameterization of Wiesenburg and Guinasso (1979) and Weiss and Price (1980) for CH_4 and N_2O, respectively. GHG flux through the air–sea interface was determined using the following equation, modified by Wanninkhof (1992):

$$F = \mathrm{kw}(T^{\circ},\ \mathrm{salinity}) \cdot (C_w - C_a)$$

where kw is the transfer velocity from the surface water to the atmosphere, as a function of wind speed and temperature and salinity from the mixed layer according to parametrization, C_w is the mean gas concentration in the mixed layer, while C_a is the gas concentration in the mixed layer expected in equilibrium with the atmosphere. Since gas transfer velocity is related to wind speed, this was calculated according to the well-known exchange models of Liss and Merlivat (1986) or LM86 and Wanninkhof (1992) or W92, based on the dependence of the transfer velocity on wind speed. Wind speed and direction were obtained from an onboard register using the ship's meteorological station as per international protocols. Wind speed was estimated as a moving average

BGD
11, 12531–12569, 2014

of seven days before the sampling (stations) in order to smooth out short-term fluctuations and highlight longer-term trends. The mixed layer depth was calculated using a potential density-based criterion, defining the mixed layer depth (ML) as the shallowest depth at which density increased by 0.02 kg m^{-3} from the sea surface value.

Pearson product-moment correlations (rs) were determined for GHG, TChl *a* and nutrient inventories estimated in the ML and in the whole water column (WC). The threshold value for statistical significance was taken as $p < 0.05$. A principal component analysis (PCA) using the empirical orthogonal function (EOF; Emery and Thomson, 1997) was performed to find the co-variability patterns of a number of stations located in spatial gradients in terms of nutrients, gases (O_2, N_2O, and CH_4) and Chl *a*. In addition, dissolved Fe content was used as a qualitative variable according to data obtained during the KEOPS 2 cruise (Quéroué et al., 2014), 1 being low availability, 2 moderate and 3 high (Blain et al., 2014). The PCA was made by transect (W–E and N–S transects) and by layer in the water column from the surface to 500 m and from the surface to the base of the mixed layer.

3 Results

3.1 Oceanographic conditions

Oceanographic characteristics of the sampled stations during the KEOPS 2 cruise are shown in Table 1. Two transects, almost synoptically made across and along the KPR (survey region – Fig. 1) were undertaken to establish the position of the main mesoscale structures as fronts (Fig. 2). The north and south PFs (hereafter NPF and SPF, respectively) crossing the KPR and their associated convergence processes were observed by temperature and salinity gradients, similar to those observed along the W–E transect (47° S). Figure 2 shows these physical structures.

Figure 2a and b shows vertical cross sections along the N–S transect of temperature (from 1.67° to 4.17 °C) and salinity (from 33.67 to 34.68). These distributions

BGD
11, 12531–12569, 2014

coincided with the expected water mass distribution, this being the case of the northern (Sts. TNS01-02) and southern (Sts. A3, TNS10) stations, mainly occupied from the surface to 250 m by the SAMW and the AASW, respectively. A gradual decrease in temperature and an increase in salinity were observed in the surface layer from north to south. These variables also marked the presence of a mesoscale structure around 49° S, where the most southeastern stations (Sts. TNS10 and A3) are located at the edge of the southern part of the plateau. There intense vertical and lateral advection of the bottom water enriched in dissolved Fe and even lithogenic silicate provoked a relatively permanent and recurrent phytoplankton bloom (Blain et al., 2007). There was a tongue of colder and fresher water mass (compared to surrounding waters) spreading northward in subsurface waters. This was an expression of the PF, which marked the location where the AASW moving northward descended rapidly and sank below a depth of 200 m (Fig. 2a and b).

Figure 2c and d shows vertical cross sections along the W–E transect (66° to 75° E) of temperature (varying between 2.41° and 3.3 °C) and salinity (varying between 33.60 and 34.67). A tenuous structure with colder and fresher surface waters was registered in the FP, which crossed these transects twice, at 71° E (St. TWE03-04 or NPF) and at 73.5° E (StTWE07-08 or SPF). Middle stations (Sts. TWE04, -05 and E) demarked an area of a complex recirculatory system in a stationary meander of the PF, hereafter the Central Section. This section is bathed by mixed Antarctic surface water (AASW) and coincides with the area with the PF northward inflexion (Fig. 1). The presence of Subantarctic mode water (SAMW) was observed east of 73.5° E (Sts. TWE07-08, Fig. 2e).

A T-S diagram (Fig. 2e and f) illustrates the spatial dominance of the two main water masses in the water column in the W–E and N–S transects. The T-S diagram shows gradual mixing from the warm (> 4 °C) and saline (> 34.6) SAMW, northward and westward of the PF, to the cool (< 2 °C) and fresh (< 33.6) AASW (southern of the PF, Table 1). In addition, a marked variability in subsurface water was observed, ascribed to mixing water masses. This was strongly pronounced in the W–E transect, in which the

BGD
11, 12531–12569, 2014

eastern most stations (within the PF) revealed a strong vertical mixing process produced by convergence, particularly evident at TWEO7 (Fig. 2f). T-S diagrams clearly separated stations located to the north of the PF within the SAMW (Sts. TNS01-02) from those located to the south of the PF (Sts. TNS09-10 and A-3).

3.2 Biogeochemical variables

Figure 3 shows vertical cross sections along the W–E transect of biogeochemical variables including nutrients, TChl *a* and GHGs. The surface layer continuously showed elevated NO_3^- concentrations, fluctuating from 22 to 27 µmol L^{-1} (typical condition of the AASW). However, consumption of this nutrient east of 73.5° E was observed. PO_4^{3-} presented the same pattern as NO_3^- and the N : P ratio of dissolved nutrients averaged around 14.5, with the exception of some values of 13.2 from stations located at the NPF and SPF (Fig. 3e and f). These patterns coincided with a pronounced increase in TChl *a*, relative to those in the western (within coastal waters close to the Kerguelen Island) and Central Section (Fig. 3b). In fact, TChl *a* fluctuated from 0.005 to 4.7 µg L^{-1} and peaked at Sts. TWE01 and TWE07. The observed pattern (Lasbleiz et al., 2014) matched significantly with the dissolved Fe spatial distribution reported by Quéroué et al. (2014).

Nitrous oxide fluctuated from 14.0 to 25.4 nmol L^{-1} (equivalent to a range of 102–182.2 % saturation). N_2O concentration was close to equilibrium with the atmosphere in surface waters in the western and central section (70.5–73° E) and slightly undersaturated in surface water (around 90 %) in both identified PF structures, St. TWE04 or NPF and St. TWE07 or SPF (Fig. 3d). N_2O levels increased slightly to around 120 % saturation toward subsurface water. CH_4 ranged from 1.4 to 31.35 nmol L^{-1}, equivalent to a range of saturation of 43–969 %. In contrast to N_2O, surface waters were always supersaturated in CH_4, showing the highest increase in gas levels of up to 970 % in coastal waters close to Kerguelen Island, a relative decrease (< 200 %) in the central section (between 71° and 73.5° S, or Sts TWE04, 05 and E2), and a strong increase

BGD
11, 12531–12569, 2014

of up to 778 % at SPF. Remarkably, CH_4 concentrations in subsurface waters were low compared to the surface waters (Fig. 3c).

Vertical cross sections of biogeochemical variables along the N–S transect (46–51° S) are shown in Fig. 4. NO_3^- and PO_3^{4-} gradually increased from north to south from 24 to 30 µmol L^{-1} and from 1.5 to 2 µmol L^{-1}, respectively (Fig. 4e and f). This spatial trend coincided with the expected transition of water mass dominance and its mixing between the SAMW and the AASW. TChl *a* ranged from 0.005 to 2.391 µg L^{-1} and peaked in the southern most stations (Sts. TNS08, -09 and A3-2; Fig. 4b) and coincided with a slight increase in nutrients. These trends coincided with the presence of the southern limit of the KPR, where upwelling-like circulation was observed (Zhou, 2014), as indicated by temperature and salinity distribution (Fig. 2c and d). N_2O concentrations ranged from 12.37 to 23.8 nmol L^{-1}, equivalent to 88.5 to 171 % saturation. Levels close to equilibrium or undersaturation were often observed in surface waters, except at St. TNS08 (Fig. 4d). CH_4 varied from 1.47 to 21.88 nmol L^{-1}, or 45 to 666 % saturation. Notably, the same spatial patterns were found for surface CH_4 distribution, with maximum saturation up to 550 % (Fig. 4c). Chl *a* matched with the observed CH_4 in this transect. Southern stations, like St. A3 located in an area of relatively high bioavailable Fe and phytoplankton bloom had extremely low N_2O concentrations (less than 6.9 nmol L^{-1} or 70 % saturation).

PCA results were obtained from the W–E (Fig. 5a and b) and N–S transects (Fig. 5c and d). All biogeochemical variables measured in the water column came from the surface to a depth of 500 m and only from the ML. The results did not change when O_2 was removed from the analysis, indicating that this variable does not explain the variability. Stations located on the W–E transect were grouped into three sets, clearly separating stations located on the eastern section (St. TWE07) from those in the western (TWE01-02) and Central Sections. The variability among stations was explained mainly by the first component, accounting for 75.7 % of the variance. As can be noted in Fig. 5, we interpreted the possible relationships among the variables and assigned weights to all of them (illustrated with the eigenvector). The figure shows a close rela-

BGD
11, 12531–12569, 2014

tionship among N_2O and nutrients and CH_4, Fe and Chl *a*. The PCA analysis with data from the entire water column provided a similar grouping of the sampled stations.

When the PCA analysis was applied to data from the N–S transect, it captured more variation among the stations (Fig. 5c and d). In effect, the stations did not clearly group themselves (separating TNS01 from TNS10) nor did the variables reveal close relationships to each. In fact, the first two components only accounted for 39.2 % of variations, indicating gradual changes as water masses mixed (Fig. 5c and d). Some differences were found when the PC analysis was made with the data from the ML separately from the data from entire water column. These results suggest that subsurface waters, which are being sunk and advected northward, have another oceanographic signature.

3.3 Vertical distribution of gases and other variables at selected stations

Figure 6 shows typical profiles of oceanographic and biogeochemical variables (including gases). Stations were separated a priori according to biogeochemical (PCA analysis; Fig. 5) and oceanographic criteria (T-S diagram, Fig. 2e and f). Vertical distribution was compared at stations like St. R, well-known as a Fe-limited HNLC area; the southernmost station, St. A3, with quasi permanent phytoplankton bloom (historical station sampled in KEOPS 1), and with certain Fe levels (Blain et al., 2007), a northern station immersed in SAMW (TNS01) and stations within the NPF and SPF (TWE03-07), the latter had moderate Fe enrichment, respectively (Quéroué et al., 2014), as well as higher TChl *a* levels than the other stations. Stations located in the extreme point of the TWE had the highest CH_4 levels (Fig. 6), while N_2O levels were relatively low, On the other hand, Sts. TNS1 and A3, located in the extreme north and south of the N–S transect and respectively bathed by SAMW and the AASW, presented relatively low levels of CH_4 compared to the W–E transect. Station R, which is located in one of the more oligotrophic conditions of the southern ocean (special volume of KEOPS 1), had the lowest N_2O and CH_4 content and both gases were homogeneously distributed with depth (Fig. 6), this being consistent with the expected trophic condition, with TChl *a* levels of less than 0.005 µg L^{-1}. Remarkably, elevated CH_4 concentrations

BGD
11, 12531–12569, 2014

were mostly located at the ML base and decreased as depth increased, whereas N_2O concentrations gradually increased with depth.

3.4 Nutrient, TChl *a* and GHG inventories and air–sea GHG exchanges

ML depths varied widely from 16 m (at the station near Kerguelen Island) to 181 m. ML depth did not show any significant relationship to wind speed (rs: 0.20 $p = 0.41$) or the water mass structure (Table 1 and Fig. 2), but seems to be related to the complex mesoscale circulation observed in the KPR (Zhou et al., 2014).

Table 2 shows the inventories of NO_3, PO_4^{3-} and GHGs in the ML and the water column from the surface to 500 m; mean GHG concentrations in the ML, wind speed and air–sea GHG fluxes are included. The TChl *a* pool, estimated on the basis of the photic layer, fluctuated from 8.77 to 75.45 mg m^{-2}. It was notably greater at Sts. SPF and A3-2 (up to fivefold) than at more oligotrophic stations like St. R. Surface NO_3^- and PO_4^{3-} inventories, which varied from 1.56 to 16.03 and 0.13 to 1.07 mol m^{-2}, respectively, did not show significant differences among stations. Minimal values were registered at stations St. TWE07, -08 and TNS01, both located north of the PF. The N_2O pools varied from 0.201 to 2.55 and from 1.12 to 10.05 mmol m^{-2} in the ML and WC, respectively. Minimum values were registered at the ML at stations within or north of the PF. These surface pools did not significantly correlate with TChl *a*, but correlated strongly and negatively with nutrients (rs: 0.91 $p < 0.001$ for NO_3^- and rs: 0.92, $p < 0.001$ for PO_4^{3-}).

CH_4 inventories fluctuated between 0.19 and 3.31 mmol m^{-2} for the ML and 1.06 and 7.44 mmol m^{-2} for the WC. Inventories in the ML were again two and fivefold higher at St. SPF and A3-2, respectively, than at St. R. CH_4 levels in the WC as a whole were four and sevenfold higher than at St. R. The comparison of CH_4 inventories (standardized by the layer's thickness) obtained from the ML and from the entire water column put in evidence that maximum values came from the ML's base, remarkably in the PF (Table 2). CH_4 pools correlated positively with TChl *a* pools (rs = 0.69; $p < 0.05$), but did

BGD
11, 12531–12569, 2014

not show any correlation with NO_3^- and PO_4^{3-}. Thus, minimum values for both nutrients were found when TChl *a* was higher.

Average hourly wind velocity during the cruise was 10.53 ± 5.52 m s^{-1}, occasionally falling below 0.31 m s^{-1} or rising above 29.1 m s^{-1}. N_2O fluxes, estimated by LM86, fluctuated between −9.69 and 10.02 (mean: 1.25 ± 4.04 µmol m^{-2} d^{-1}), while those estimated by W92 varied from −18.69 to 20.2 µmol m^{-2} d^{-1} (mean: 2.41 ± 7.88). At high wind speeds, such as those measured during the N–S transect (21–23 October 2011, mean value of 12.08 m s^{-1}) compared to those registered during the W–E transect (31 October–2 November, mean value of 5.61 m s^{-1}), substantial differences were observed between the cubic (LM86) and the quadratic parameterizations (W92). The latter increased in calculated fluxes by approximately a factor of two at high wind speeds, while at low wind speeds the difference between LM86 and W92 was up to a factor of ∼ 1.6 (see Table 2).

CH_4 fluxes varied from 0.21 to 38.1 (mean: 10.01 ± 9.97) and from 0.32 to 70.24 (mean: 21.27±21.07) µmol m^{-2} d^{-1}, when LM86 and W92 were used, respectively. The study area acts as a source at times of very high CH_4 effluxes into the atmosphere, particularly at stations St. TNS09 and St. A3-3, where emissions were around three times as high as those calculated for St. R. There are important differences between the two parameterizations, although the same trend among stations was obtained (Table 2).

4 Discussion

4.1 Physical characteristics

The Antarctic Polar Front (PF) marks an important climate boundary in terms of oceanic heat and salt budgets and a biogeochemical frontier with respect to GHG content and air–sea GHG fluxes (like N_2O and CH_4). The PF path exhibits considerable variability, meandering and forming eddies and rings. The location of the PF is mainly determined by the movements of deep waters and is probably influenced strongly by

BGD
11, 12531–12569, 2014

topography and bathymetric features such as the Drake Passage and the Kerguelen Plateau (Sandwell and Zhang, 1989; Patterson, 2005). These structures generate relative vorticity that is likely dissipated through nonlinear processes such as data (including GHG) from the surface water confirms the separation/grouping of stations according to certain eddy action or Rossby waves (Hughes, 1995, 1996), provoking elevated eddy kinetic energy. These mesoscale structures in the study area are always associated with strong vertical and lateral mixing, as well as advection (Park and Viver, 2012; Zhou et al., 2014) that creates fertilization (by both Fe and acid silicate nutrient), therefore stimulating TChl *a* production mainly supported by the microplanktonic community (Lasbeiz et al., 2014), which in turn can affect GHG cycling. The PCA analysis conducted with biogeochemical variables showed a close relationship among CH_4, Fe and TChl *a* (Fig. 5) but for the case of N_2O, it revealed a a close relation to N nutrient, Nitrification may be responsible for N_2O production via the oxidation of hydroxylamine to nitrite and nitrate. Its dependence on a Fe-containing enzyme could locally increase N_2O production by nitrification (Morel et al., 2003). In the case of CH_4, the most likely relationship is that an increase in Fe favors Fe-containing proteins involved in electron transfer chains in bacterial respiratory systems (Kirchman et al., 2003), which in turn activate bacterioplankton metabolism (Arrieta et al., 2004).

Our findings show that stations on the shelf (TWE01-02) in the SPF (TWE07) and the southern part of the KPR (A3-1, A3-2), where there are conspicuous accumulations of particulate matter (Lasbleiz et al., 2014), had high CH_4 content (Table 2). There was a heavy CH_4 accumulation (up to 25 nmol L^{-1}, equivalent to 778 % saturation) concentrated at the pycnoclines in the SPF, representing about 500 % as much as the average level in the ML (Table 2, Figs. 3f and 4f). It is important to note that stations with high TChl *a* levels are dominated by micro-phytoplankton with high biogenic silica content (Lasbleiz et al., 2014) and therefore susceptible to being rapidly exported to the base of the mixed layer (Jouandet et al., 2014), which explains the highest CH_4 levels found.

BGD
11, 12531–12569, 2014

Remarkably, spatial distribution of N_2O contrasted in same way to observed CH_4 and TChl *a* distributions in the W–E transect. N_2O had low levels in surface waters of the SPF and at Stations A3-1 and A3-2 (less than 6.9 nmol L^{-1}, equivalent to 69 % saturation), reflecting in some way consumption by local microbiological communities that support high particle matter accumulation. The observed patterns raise questions as to why some mesoscale structures support relatively high TChl *a* levels in comparison to surrounding waters and particularly, whether there are some fertilization mechanisms (including Fe and nutrients) promoting GHG cycling and concomitant microbial activities.

In contrast to other regions where Fe input is mainly the result of eolian transport on the surface (Jickells et al., 2005), vertical mixing of deep Fe-rich seawaters is the main mechanism in the study area (Mongin et al., 2008; Zhou et al., 2014). In fact, Using Ra isotopes to trace Fe, Sanial et al. (2014) indicated that Fe could be supplied from sedimentary sources, as well as laterally advected from the southern region of Heard Island and exchanged through the Polar Front. Similar results were found with the rare earth tracer (Queroue et al., 2014) and during Keops 1 by Zhang et al. (2008) and Maraldi et al. (2009).

4.2 The case of N_2O

Fuhrman and Capone (1991) pointed out that stimulating ocean productivity by Fe addition, which enhances nitrogen export from the euphotic zone to the subsurface layer, can result in enhanced N_2O formation via stimulated nitrification. Since N_2O is a powerful greenhouse gas, 300 times more radiative than CO_2 per molecule, Fe addition could counteract the climatic benefits of atmospheric CO_2 drawdown (Jain et al., 2000). The link between Fe fertilization and enhanced N_2O formation was supported by the study of Law and Ling (2001), who found a small but significant N_2O accumulation in the pycnoclines in summer during the Southern Ocean Iron Enrichment Experiment (SOIREE) at 61° S, 140° E. Jin and Gruber (2003) subsequently predicted the long-term effect of Fe fertilization on global oceanic N_2O emissions using a coupled

BGD
11, 12531–12569, 2014

physical-biogeochemical model. Based on the model outputs, they concluded that Fe fertilization induced N_2O emissions that could offset the radiative benefits of the CO_2 drawdown.

However, during other Southern Ocean Iron Enrichment Experiments (EIFEX), Walter et al. (2005) found no N_2O enrichment after artificial Fe fertilization. As observed in the EW transect (Fig. 3), natural Fe fertilization did not seem to stimulate N_2O accumulation in surface and subsurface water. Dividing the E–W transect into three sections according to PCA analysis, these sections did not show significant differences among their ML N_2O inventory with respect to those estimated for St. R, which was used as a reference station (Table 2). Contrary to what was expected, an increase in N_2O content was not observed at stations close to Kerguelen Island (western section) highly enriched by Fe from fresh water and sediments. This trend suggests that nitrifiers are not being stimulated by Fe supply from the sediments. Remarkably, the St. SPF and A2-3 was in equilibrium and slightly depleted in N_2O (Fig. 3e; Table 2). The only plausible explanation is that mixing process produced in the SPF (which have moderate Fe levels and TChl *a*) may stimulate the N fixers, as demonstrated by Mills et al. (2004), Berman-Frank et al. (2007) and Moore et al. (2009). N-fixing microorganisms may have an effect on N_2O inventory as they could be used as an alternate substrate for fixers, as suggested by Farias et al. (2013). Thus, biological N fixation could consume N_2O, producing an N_2O deficit or undersaturation. Coincidently, St. SPF also had the highest surface N-fixation (Gonzalez et al., 2014), suggesting that N_2O is used as substrate by diazotrophs (Farias et al., 2013) and that this process is stimulated by enhanced Fe supply. N_2O undersaturation or equilibrium with the atmosphere was observed in the N–S transect (Fig, 4e), particularly at stations north of the PF bathed by SAMW. This suggests that some process is removing or consuming this gas in the upper water column. A notable level of subsaturation was also observed at St. A3-2, which is located in recurring phytoplankton bloom and in a regime of relatively high Fe availability due to the presence of the Plateau (Blain et al., 2007). The exception was St. TNS08, located

BGD
11, 12531–12569, 2014

on a mesoscale structure (Fig. 2c), which had slight N_2O supersaturation (~ 120 %) (Fig. 4e).

N_2O undersaturation has been reported, although rarely, in Polar and Sub-polar Ocean regions (Butler et al., 1989; Law and Ling, 2001; Foster et al., 2009). However, there is no convincing explanation for undersaturation, which would go against the enhanced solubility of gases due to low seawater temperatures. Gas solubility in surface waters depends on temperature and salinity. If these physical variables change in less time than that required for equilibrium of gases with the atmosphere, there may be a gas deficit. Thus, deviation from the equilibrium condition could be caused by rapid heating or cooling, refreshing and/or a mixing of water masses (Sarmiento and Gruber, 2006). An analysis of these potential changes was made for the AASW and the SAMW. Cooling of more than 3 °C or freshening of up to 10 is required to produce the observed undersaturation, neither of which was observed during the sampling (Table 1) or expected during the season (Park and Viver, 2012). Additionally, if the two water masses were mixed proportionally, as they are, the resulting process cannot produce undersaturation regarding the original N_2O levels and their temperature and salinity signature. Thus, a preliminary analysis indicates biological processes are responsible for N_2O undersaturation and the concomitant influx from the atmosphere. In contrast, subsurface waters have higher N_2O concentrations (saturations from 120 % to 180 %) than surface, which indicates a net accumulation. The plausible process responsible for N_2O accumulation there is aerobic ammonium oxidation (Codispoti et al., 2001), but no significant difference was noted at the stations with the highest TChl *a* levels, indicating that N_2O production by nitrification was not substantially stimulated at those stations.

4.3 The case of CH_4

CH_4-producing microorganisms are thought to require strictly anoxic conditions, which are found in O_2-deficient waters, sediments or particles. Since oxygen-deficient waters are not expected in the well-mixed and cold southern Ocean (Figs. 3b and 4b),

BGD
11, 12531–12569, 2014

methanogenesis via anaerobic organic matter respiration is precluded. Thus, CH_4 production in surface waters should only occur in association with anoxic particles (Karl and Tilbrook, 1994) or via the degradation of organic methyl compounds.

There have been few studies on CH_4 distribution and production in the Southern Ocean. Wingenter et al. (2004) found low levels of CH_4 production (less than 1 % of that increase) during artificial Southern Ocean iron enrichment experiments (SOFex). Simulated large-scale Southern Ocean Fe fertilization (OIF) also resulted in anoxic conditions favoring anaerobic methanogenesis (Oschlies et al., 2010). However, our results show that waters of the WE transect were strongly enriched in CH_4 by a factor of 4 (Fig. 3e), associated mainly with elevated TChl *a* levels. A different pattern was observed at the SPF and the southeastern bloom stations (St. A3-2), where high levels of CH_4 accumulation were associated with elevated phytoplankton biomass production and moderate Fe enrichment (Queroue, 2014). The fact that the western and eastern sections showed high Fe levels (Queroue, 2014) relative to the central part of the W–E transect, and that these sections had high CH_4 levels suggests that Fe promotes CH_4 production.

It is important to note that high TChl *a* levels were associated with high primary production (PP) rates of the phytoplankton bloom, as shown by Cavagna et al. (2014). For example, station A3-2 and SPF (maximum TChl *a*) had the highest integrated primary production rates (up to 3380 $mg\,m^{-2}\,d^{-1}$) and the lowest C export level of around 2–3 %, (Cavagna et al., 2014) suggests an intense level of PP supported by regenerated N sources. There was a lower rate of regenerated production at the St. R (with a PP rate of around 135 $mg\,m^{-3}\,d^{-1}$ and an exported C rate of around 25 % of PP).

Phytoplankton bloom should stimulate bacterioplankton activity or create a proportional amount of organic particles that can host anoxic microhabitats for CH_4-producing bacteria. In fact, Christaki et al. (2014) showed that the highest bacterial production rates (up to 110 $mg\,C\,m^{-2}\,d^{-1}$) and the greatest abundance of heterotrophic bacteria were associated with stations with phytoplankton bloom (SPF and A3-2). This pattern suggests a close relationship between phytoplankton or microbial activity and photo-

BGD
11, 12531–12569, 2014

synthesis, which may be recycling of DMSP/DMS. In this sense, the substantial production of DMSP and DMS was repeatedly observed in Fe enrichment experiments (Turner et al., 2004). Fertilization experiments in the Southern Ocean related to short-term (several weeks) atmospheric dust-related iron supply have shown that DMS concentrations increase when Fe is added artificially in small patches to iron-limited regions. However, during KEOPS 1 Belviso et al. (2008) found that the massive summer phytoplanktonic bloom sustained by natural fertilization in the KPR was not a substantially larger source of DMS than the surrounding HNLCarea. The sustained enrichment of Fe in the KPR did not translate into an increase in DMS, which may be due to a high turnover of DMS/DMSP. Although the dynamic response might not be sustained in long-term Fe fertilization, as observed seasonally in the KPR (Blain et al., 2007), DMS/DMSP substrates could be used to generate CH_4 in the water column.

The most convincing explanation was the lack of transfer efficiency of DMSP to DMS due to the higher levels of bacterial production measured over the KPR during the last phase of phytoplankton bloom (austral summer) (Belviso et al., 2008). In the same way, Bopp et al. (2008), using a 3-D ocean biogeochemical model, reproduced the observed decoupling between high productivity and DMS rich waters as a consequence of variable S to C ratios in phytoplankton, the transfer efficiency from the DMS precursor to DMS, and the bacterial DMS-consumption rate.

Nano-phyto-bacterioplankton relationships control DMS turnover, which could result in several mechanisms of DMSP/DMS degradation (Simó et al., 2002; Vila-Costa et al., 2006) and produce CH_4 (Damm et al., 2010; Florez-Leiva et al., 2013; Weller et al., 2013). Increased grazing of microbes by microzooplankton, as observed by Christaki et al. (2014) may contribute to particle recycling (rich in organic carbon and DMSP) and increase the potential for methanogenesis (Weller et al., 2013). These authors showed that phytoplankton species composition and biomass in different bloom phases, as well as eddy dynamics, were important determinants of CH_4 saturation and emission. Our results showed that the marked differences in CH_4 content measured in the W–E and N–S transect (t-student: 3.21 $p < 0.001$) (Figs. 3f and 4f) generally coincided with areas

BGD
11, 12531–12569, 2014

of relatively higher Fe availability, which in turn favors PP, as was found in frontal and eddy structures. Likewise, the CH_4 accumulation at pycnoclines (Fig. 6) indicates that most CH_4 came from accumulated particles sinking from the surface water. Among heterotrophic microorganisms DMS degradation can be ascribed to methylotrophic bacteria (Vissher et al., 1994) that derive energy from the conversion of methyl into other products, as well as using S as a source for methionine biosynthesis (Kiene et al., 1999). Current studies of natural and cultivated SAR11 alphaproteobacteria (strain Ca. P. ubique HTCC1062; Sun et al., 2011) indicate that these microorganisms, among the most abundant heterotrophic bacteria in surface waters, possess genes that encode for oxidation pathways of a variety of one-carbon compounds, and have the capacity for demethylation and C1 oxidation, but do not incorporate C1 compounds as biomass. Thus, methylotrophs are candidates for mediated CH_4 generation (Florez-Leiva et al., 2013; Weller et al., 2013).

These vertical profiles indicate that most CH_4 is being formed at the surface and euphotic layers and consumed at subsurface and intermediary depths (Fig. 6). Thus, CH_4 distribution appears to be controlled largely by biological mechanisms rather than mixing, except in front structures like those observed in the St. TWE07, where downwelling and intense mixing occur (see Fig. 2). CH_4 undersaturation, fluctuating between 40 and 90 %, was found in most sampled stations at depths of > 200. It is unlikely that undersaturation results from the entrainment of CH_4-depleted waters that have high levels of gas solubility. More likely a biological mechanism is involved. The only known process able to consume CH_4 is methanotrophy, and the fact that subsurface waters were depleted of CH_4 suggests that CH_4 consumption is higher than production or that no production occurs in subsurface waters. Interestingly, although CH_4 microbial oxidation occurs throughout the water column and is recognized as an important process that reduces CH_4 emissions (Reeburgh et al., 2007; Rehder et al., 1999), microbial communities mediating aerobic CH_4 oxidation have scarcely been investigated. There have been few measurements of aerobic CH_4 oxidation in marine environments and measurement taken of open systems under oligotrophic regimes (Tilbrook and Karl,

BGD
11, 12531–12569, 2014

1994; Holmes et al., 2000) have found lower levels of oxidation than in the oxic/anoxic interface (Sansone and Martens, 1978; Reeburgh et al., 1991).

4.4 CH_4 and N_2O emission in the Southern Ocean

Very dynamic gas exchanges were registered in the KPR, with source and sink scenarios for N_2O and just a source scenario for CH_4. Given highly variable wind velocities, with averages not exceeding 14 m s^{-1}, LM86 was the more appropriate approach to calculate air–sea gas fluxes.

Since ML depth did not correlate to wind speed (rs: 0.31, $p < 0.05$), the gas inventories in the ML reflect not only the effect of wind stress, supplying gases and nutrients into the ML, but also advection related to mesoscale structures, in the central part of the WE transect where a stationary meander was observed (Zhou et al., 2014). In fact, CH_4 fluxes were higher at stations located at the PF and A3, where phytoplaktonic blooms were observed (see Table 2), but the tendency was the reverse for N_2O, with an influx in the aforementioned stations. CH_4 emission rates during this study (Table 2) were higher than previous measurements, with a range of 0.1 to 3. µmol m^{-2} d^{-1} for the Pacific Ocean (Bates et al., 1996; Holmes et al., 2000; Sansone et al., 2001) and 0.5 to 9.7 µmol m^{-2} d^{-1} for the Atlantic Ocean (Oudot et al., 2002; Forster et al., 2009). Excluding stations located at the polar front with other phytoplaktonic blooms (Sts, TWE07 and A3), the average for CH_4 emissions was 25 % lower.

In the case of N_2O, the estimates in this study were in the range expected for the oligotrophic open ocean (Nevinson et al., 1995). N_2O subsaturation and its concomitant influx were registered; although this situation has not yet been well described for the Southern Ocean. N_2O sinks can occasionally be observed (Butler et al., 1989; Law and Ling, 2001), the most plausible explanation for which is N_2O assimilation by N-fixing microorganisms. This process may be responsible for the estimated N_2O influx.

BGD
11, 12531–12569, 2014

5 Implications

Mesoscale structures mainly associated with the polar front, and meanders and filaments were clearly observed at all temperatures and chlorophyll levels, and with CH_4. This study suggests that mesoscale structures play a significant role in surface CH_4 production and subsequent air–sea gas exchange. This was not found in the case of artificial fertilization experiments, indicating that the turnover and evolution of microbial communities in this structure are fundamental for the development of substrates and conditions for CH_4 regeneration. N_2O does not spatially respond to natural stimulation, at least in terms of N_2O production (nitrification). Some insight into N fixation may have been provided, but further study is needed. The timing and nature of microbial activity involved in OM production and its concomitant exportation and/or degradation, which could affect the microbial activity involved in GHG cycling, seems to be different with natural fertilization.

Acknowledgements. We thank the captain and crew of the R/V *Marion Dufresne*. We are also grateful to Louise Oriol and Stephane Blain for nutrient data and Marine Lasbleiz for HPLC analysis of chlorophyll measurements. We also recognize all our colleagues that contributed to KEOPS 2. CF and LF were supported by Proyecto Ecos-Conicyt C09B02 and the International Associated Laboratory MORFUN. LF financed the analysis of samples obtained in the Keops 2 cruise with FONDECYT N° 1120719. This is a contribution by 15110009 (FONDAP-CONICYT).

References

Arrieta, J. M., Weinbauer, M. G., Lute, C., and Hernd, G. J.: Response of bacterioplankton to iron fertilization in the Southern Ocean, Limnol. Oceanogr., 49, 799–808, 2004.

Bates, T. B., Kelly, K. C., Johnson, J. E., and Gammon, R. H.: A re-evaluation of the open ocean source of methane to the atmosphere, J. Geophys. Res., 101, 6953–6961, 1996.

Berman-Frank, I. Quigg, A., Finkel, Z. V., Irwin, A. J., Haramaty, L.: Nitrogen-fixation strategies and Fe requirements in cyanobacteria, Limnol. Oceanogr., 52, 2260–2269, 2007.

BGD
11, 12531–12569, 2014

Blain, S., Quéguiner, B., Armand, L., Belviso, S., Bombled, B., Bopp, L.,Bowie, A., Brunet, C., Brussaard, K., Carlotti, F., Christaki, U., Corbiére, A., Durand, I., Ebersbach, F., Fuda, J. L., Garcia, N., Gerringa, L. J. A., Griffiths, F. B., Guigue, C., Guillerm, C., Jacquet, S., Jeandel, C., Laan, P., Lefevre, D., Lomonaco, C., Malits, A., Mosseri, J., Obernosterer, I., Park, Y. H., Picheral, M., Pondaven, P., Remenyi, T., Sandroni, V., Sarthou, G., Savoye, N., Scouarnec, L., Souhault, M., Thuillers, D., Timmermans, K. R., Trull, T., Uitz, J., Van-Beek, P., Veldhuis, M. J. W., Vincent, D., Viollier, E., Vong, L., and Wagener, T.: Effect of natural iron fertilization on carbon sequestration in the Southern Ocean, Nature, 446, 1070–1075, 2007.

Blain, S., Sarthou, G., and Laan, P.: Distribution of dissolved iron during the natural iron fertilization experiment KEOPS (Kerguelen Plateau, Southern Ocean), Deep-Sea Res. II, doi:10.1016/j.dsr2.2007.12.028, 2008.

Blain, S., Oriol, L., Capparos, J., Gueneugués, A., and Obernosterer, I.: Distribution and stoechoimetry of dissolved nitrogen and phosphorus in the iron fertilized region near Kerguelen (Southern Ocean), Biogeosciences Discuss., KEOPS 2 special issue, 2014.

Belviso, S., Bopp, L., J. Mosseri, M. Tedetti, J., Garcia, N., Griffiths, B., Joux, F., Obernosterer, I., Sempéré, R., Uitz, J., and Velhuis, M.: Effect of natural iron fertilisation from below on the distribution of DMS and DMSP in the Indian sector of the Southern Ocean, Deep Sea Res. Pt. II, 55, 893–900, 2008.

Bopp, L., Belviso, S., Aumont, O., and Blain, S.: Modeling the effect of iron fertilization on dimethylsulfide emissions in the Southern Ocean, Deep Sea Res. Pt. II, 55, 901–912, 2008.

Butler, J. H., Elkins, J. W., Thompson, T. M., and Egan. K. B.: Tropospheric and dissolved N_2O of the West Pacific and East Indian Oceans during the El Niño Southern Oscillation event of 1987, J. Geophys. Res., 94, 14865–14877, 1989.

Cavagna, A. J., Lefèvre, D., Dehairs, F., Elskens, M., Fripiat, F., Closset, I., Laslbleiz, M., Florez-Leiva, L.,Cardinal, D., Leblanc, K., Fernandez, C, Oriol, L.,Blain, S., and Quéguiner, B.: Production regime and potential for carbon export in the naturally iron fertilized Kerguelen area (Southern Ocean). Biological productivity regime in the surface water around the Kerguelen Island in the Southern Ocean – From the use of an integrative approach, Biogeosciences Discuss., KEOPS 2 special issue, 2014.

Charpentier, J., Farías, L., and Pizarro, O.: Nitrous oxide fluxes across eastern South Pacific gyre, Global Biogeochem. Cy., 24, doi:10.1029/2008GB003388, 2010.

Christaki, U., Lefèvre, D., Georges, C., Colombet, J., Catala, P., Courties, C., Sime-Ngando, T., Blain, S., and Obernosterer, I.: Microbial food web dynamics during spring phytoplankton

BGD
11, 12531–12569, 2014

blooms in the naturally iron-fertilized Kerguelen area (Southern Ocean), Biogeosciences Discuss., 11, 6985–7028, doi:10.5194/bgd-11-6985-2014, 2014.
Cicerone, R. J. and Oremland, R. S.: Biogeochemical aspects of atmospheric methane, Global Biogeochem. Cy., 2, 299–327, 1988.
Codispoti, L. A. and Christensen, J. P.: Nitrification, denitrification and nitrous oxide cycling in the eastern Tropical South Pacific Ocean, Mar. Chem., 16, 277–300, 1985.
Codispoti, L. A., Brandes, J. A. Christensen, J. P., Devol, A. H., Naqvi, S. W. A., Paerl, H., and Yoshinari, T.: The oceanic fixed nitrogen and nitrous oxide budgets: moving targets as we enter the anthropocene?, Sci. Mar., 65, 85–105, 2001.
Damm, E., Helmke, E., Thoms, S., Schauer, U., Nöthig, E., Bakker, K., and Kiene, R. P.: Methane production in aerobic oligotrophic surface water in the central Arctic Ocean, Biogeosciences, 7, 1099–1108, doi:10.5194/bg-7-1099-2010, 2010.
d'Ovidio, F., Zhou, M., Park, Y. H., Nencioli, F., Resplandy, L., Doglioli, A., Petrenko, A., Blain, S., and Queguiner, B.: Guiding biogeochemical campaigns with high resolution altimetry: waiting for the SWOT mission, in: Proceedings of 20 Years of Progress in Radar, Altimetry Symposium, Venice, Italy, 2012.
Emery, W. J. and Thomson, R. E.: Data Analysis Methods in Physical Oceanography, Pergamon Press, 634 pp., 1997.
Farías, L., Fernández, C., Faúndez, J., Cornejo, M., and Alcaman, M. E.: Chemolithoautotrophic production mediating the cycling of the greenhouse gases N_2O and CH_4 in an upwelling ecosystem, Biogeosciences, 6, 3053–3069, doi:10.5194/bg-6-3053-2009, 2009.
Farias, L., Faundez, J., Fernadez, C., Cornejo, M., Sanhueza, S., and Carrasco, C.: Biological N_2O fixation in the eastern South Pacific ocean, PLoS One, 8, e63956, doi:10.1371/journal.pome0063956, 2013.
Florez-Leiva, L., Damm, E., and Farías, L.: Methane production induced by methylsulfide in surface water of an upwelling ecosystem, Prog. Oceanogr., doi:10.1016/j.pocean.2013.03.005, 2013.
Forster, G., Upstill-Goddard, R. C., Gist, N., Robinson, C., Uher, G., and Woodward, E. M.: Nitrous oxide and methane in the Atlantic Ocean between 50° N and 52° S: latitudinal distribution and sea-to-air flux, Deep-Sea Res. Pt. II, 56, 964–976, 2009.
Fuhrman, J. A. and Capone, D. G.: Possible biogeochemical consequences of ocean fertilization, Limnol. Oceanogr., 36, 1951–1959, 1991.

BGD
11, 12531–12569, 2014

Grasshoff, J.: Methods of seawater analysis, in: Methods of Seawater Analysis, edited by: Grasshoff, K., Ehrhardt, M., and Kremling, K., Verlag Chimie, Germany, 1983.
González M. L. L., Florez-Leiva, L., Oriol, L., Cavagna, A. J., Molina, V., Farias, L., and Fernández, C.: Dinitrogen fixation in a naturally fertilized area: case of study in the Kerguelen plateau, KEOPS 2 special issue, in prep., 2014.
Hanson, R. S. and Hanson, T. E.: Methanotrophic bacteria, Microbiol. Mol. Biol. R., 60, 439–471, 1996.
Holmes, M. E., Sansone, F. J., Rust, T. M., and Popp, B. N.: Methane production, consumption, and air–sea exchange in the open ocean: an evaluation based on carbon isotopic ratios, Global Biogeochem. Cy., 14, 1–10, 2000.
Holmes, R. H., Aminot, A., Kérouel, R., Hooker, B. A., and Peterson, J.: A simple and precise method for measuring ammonium in marine and freshwater ecosystems, Canad. Fish. Aquat. Sci., 56, 1801–1808, 1999.
Hughes, C. W.: Rossby waves in the southern ocean: a comparison of TOPEX/POSEIDON altimetry with model predictions, J. Geophys. Res., 100, 15933–15950, 1995.
Hughes, C. W.: The Antarctic circumpolar current as a waveguide for Rossby waves, J. Phys. Oceanogr., 26, 1375–1387, 1996.
IPCC Climate Change: The Physical Science Basis: Working Group I Contribution to the Fourth Assessment Report of the IPCC (Climate Change 2007), edited by: Tignor, M. and Miller, H. L., Cambridge University Press, 2007.
Jain, A. K., Briegleb, B. P., Minschwaner, K., and Wuebbles, D.: J. Radiative forcing and global warming potentials of 39 greenhouse gases, J. Geophys. Res., 105, 20773–20790, 2000.
Jickells, T. D., An, Z. S., Andersen, K. K., Baker, A. R., Bergametti, G., Brooks, N., Cao, J. J., Boyd, P. W., Duce, R. A., Hunter, K. A., Kawahata, H., Kubilay, N., laRoche, J., Liss, P. S., Mahowald, N., Prospero, J. M., Ridgwell, A. J., Tegen, I., and Torres, R.: Global iron connections between desert dust, ocean biogeochemistry, and climate, Science, 308, 67–71, 2005
Jin, X. and Gruber, N.: Offsetting the radiative benefit of ocean iron fertilization by enhancing N_2O emissions, Journal Geophysical Research, 30, 2249, doi:10.1029/2003GL018458, 2003.
Jouandet, M.-P., Jackson, G. A., Carlotti, F., Picheral, M., Stemmann, L., and Blain, S.: Rapid formation of large aggregates during the spring bloom of Kerguelen Island: observations and model comparisons, Biogeosciences Discuss., 11, 4949–4993, doi:10.5194/bgd-11-4949-2014, 2014.

BGD
11, 12531–12569, 2014

Karl, D., Beversdorf, L., Björkman, K. M., Church, M. J., Martinez, A., DeLong, E. F.: Aerobic production of methane in the sea, Nat. Geosci., 1, 473–478, 2008.
Karl, D. M. and Tilbrook, B. D.: Production and transport of methane in oceanic particulate matter, Nature, 368, 732–734, 1994.
Kiene, R. P., Linn, L. J. J., Gonzalez, J. M. A., Moran, M.A., and Bruton, J. A.: Dimethylsulfoniopropionate and methanethiol are important precursors of methionine and protein-sulfur in marine bacterioplankton, Appl. Environ. Microb., 65, 4549–4558, 1999.
Kirchman, D. I., Hoffman, K. A., Weaver, R., and Hutchins, D. A.: Regulation of growth and energetics of a marine bacterium by nitrogen source and iron availability, Mar. Ecol.-Prog. Ser., 250, 291–296, 2003.
Lasbleiz, M., Leblanc, K., Blain, S., Ras, J., Cornet-Barthaux, V., Hélias Nunige, S., and Quéguiner, B.: Pigments, elemental composition (C, N, P, Si) and stoichiometry of particulate matter, in the naturally iron fertilized region of Kerguelen in the Southern Ocean, Biogeosciences Discuss., 11, 8259–8324, doi:10.5194/bgd-11-8259-2014, 2014.
Law, C. and Ling, R.: Nitrous oxide flux and response to increased iron availability in the Antarctic Circumpolar Current, Deep-Sea Res. Pt. II, 48, 2509–2527, 2001.
Liss, P. S. and Merlivat, L.: Air–sea gas exchange rates: introduction and synthesis, in: The Role of Air–Sea Exchange in Geochemical Cycling, edited by: Buat-Menard, P., D. Reidel, Dordrecht, 113–127, 1986.
Nevison, C., Weiss, R., and Erickson III, D. J.: Global oceanic emissions of nitrous oxide, J. Geophys. Res., 100, 15809–15820, 1995.
Nevison, C., Butler, J. H., and Elkins, J. W.: Global distribution of N_2O and the DN2O-AOU yield in the subsurface ocean, Global Biogeochem. Cy., 7, 1119, doi:10.1029/2003GB002068, 2003.
Maraldi, C., Mongin, M., Coleman, R. S., and Testut, L.: The influence of lateral mixing on a phytoplankton bloom: distribution in the Kerguelen Plateau region, Deep Sea Res. Pt. I, 56, 963–97, 2009.
Mills, M. M., Ridame, C., Davey, M., La Roche, J., and Geider, R.: Iron and phosphorus co-limit nitrogen fixation in the eastern tropical North Atlantic, Nature, 429, 292–294, 2004.
Mongin, M., Molina, E., and Trull, T.: Seasonality and scale of the Kerguelen plateau phytoplankton bloom: a remote sensing and modeling analysis of the influence of natural iron fertilization in the Southern Ocean, Deep-Sea Res. Pt. II, 55, 880–892, 2008.

BGD
11, 12531–12569, 2014

Moore, C.M, Mills, M. M., Achterberg, E. P., Geider., R. J. LaRoche, J., Lucas, M. I., McDonagh, E. L., Pan, X., Poulton, A. J., Rijkenberg, M. J. A., Suggett, D. J., Ussher, S. J., and Woodward, E. M. S.: Large-scale distribution of Atlantic nitrogen fixation controlled by iron availability, Nat. Geosci., 2, 867–871, 2009.

Morel, F. M. M. and Price, N. M.: The biogeochemical cycles of trace metals in the Oceans, Science, 300, 944, doi:10.1126/science.1083545, 2003.

Oschlies, A., Koeve, W., Rickels, W., and Rehdanz, K.: Side effects and accounting aspects of hypothetical large-scale Southern Ocean iron fertilization, Biogeosciences, 7, 4017–4035, doi:10.5194/bg-7-4017-2010, 2010.

Oudot, C., Jean-Baptiste, P. E., Fourreb, E., Mormichea, C., Guevela, M., Ternonc, J.-F., and Le Corred, P.: Transatlantic equatorial distribution of nitrous oxide and methane, Deep-Sea Res. Pt. I, 49,1175–1193, 2002.

Park, Y.-H. and Viver, F.: Circulation and hydrography over the Kerguelen Plateau, Mar. Ecosyst. Fish., 5, 43–55, 2012.

Patterson, S. L.: Surface Circulation and kinetic energy distributions in the Southern Hemisphere oceans from FGGE drifting Buoys, J. Phys. Oceanogr., 15, 865–884, 2005.

Quéroué, F., Sarthou, G., Chever, F., van der Merwe, P., Lannuzel, D., Townsend, A., Bucciarelli, E., Planquette, H., Cheize, M., Blain, d'Ovidio, F., and Bowie, A.: A new study of natural Fe fertilization processes in the 2 vicinity of the Kerguelen Islands (KEOPS 2 experiment), KEOPS 2 special issue, in preparation, 2014.

Reeburgh, W. S., Ward, B. B., Whalen, S. C., Sandbeck, K. A., Kilpatrick, L. J., and Kerkhof, K.: Black Sea methane geochemistry, Deep-Sea Res. Pt. II, 38, S1189–S1210, 1991.

Reeburgh, W. S.: Oceanic methane biogeochemistry, Chem. Rev., 107, 486–513, 2007.

Rehder, G., Keir, R. S., Suess, E., and Rhein, M.: Methane in the northern Atlantic controlled by microbial oxidation and atmospheric history, Geophys. Res. Lett., 26, 587–590, 1999.

Rees, A. P., Owens, N. J. P., and Upstill-Goddard, R. C.: Nitrous oxide in the Bellingshausen Sea and Drake Passage, J. Geophys. Res., 102, 3383–3391, 1999.

Rhee, T. S., Kettle, A. J., and Andreae, M. O.: Methane and nitrous oxide emissions from the ocean: a reassessment using basin-wide observations in the Atlantic, J. Geophys. Res., 114, D12304, doi:10.1029/2008JD011662, 2009.

Sandwell, D. T., and Zhang, B.: Global mesoscale variability from the Geosat exact repeat mission: correlation with ocean depth, J. Geophys. Res., 94, 17971–17984, doi:10.1029/JC094iC12p17971, 1989.

BGD
11, 12531–12569, 2014

Sanial, V., van Beek, P., Lansard, B., Souhaut, M., Kestenare, E., and d'Ovidio, F.: Radium isotopes to track sediments-derived inputs of the Kerguelen Plateau, Biogeosciences, KEOPS2 special issue, in preparation, 2014.
Sansone, F. J. and Martens, C. S.: Methane oxidation in Cape Lookout Bight, North Carolina, Limnol. Oceanogr., 23, 349–355, 1978.
Sansone, F. J., Popp, B. N., Gasc, A., Graham, W., and Rust, T. M.: Highly elevated methane in the eastern tropical North Pacific and associated isotopically enriched fluxes to the atmosphere, Geophys. Res. Lett., 28, 4567–4570, 2001.
Sarmiento, J. L. and Gruber, N.: Ocean Biogeochemical Dynamics, Princeton University Press, 2006.
Scranton, M. I. and Brewer, P.: Occurrence of methane in the near-surface waters of the western subtropical North Atlantic, Deep-Sea Res., 24, 127–138, 1977.
Simó, R., Archer, S. D., Pedró-Alió, C., Gilpin, L., and Stelfox-Widdicombe, C. E.: Coupled dynamics of dimethyl- sulfoniopropionate and dimethylsulfide cycling and the microbial food web in surface waters of the North Atlantic, Limnol. Oceanogr., 47, 53–61, 2002.
Sun, J., Steindler, L. J., Thrash, C., Halsey, K. H., Smith, D. P., Carter, A. E., Landry, Z. C., and Giovannoni, S. J.: One carbon metabolism in SAR11 pelagic marine bacteria, PloS One, doi:10.1371/journal.pone.0023973, 2011.
Tilbrook, E. D. and Karl, D. M.: Dissolved methane distributions, sources, and sinks in the western Bransfield Strait, Antarctica, J. Geophys. Res., 99, 16383–16393, 1994.
Tréguer, P.: Le Corre P Manuel d'analyse des sels nutritifs dans l'eau de mer Uti:lisation de 1'AutoAnalyzt-r 2 Technicon, 2nd edn., Univ Bretagne occidentale, Brest, 1975.
Turner, S. M., Harvey, M. J., Law, C. S., Nightingale, P. D., and Liss, P. S.: Iron-induced changes in oceanic sulfur biogeochemistry, Geophys. Res. Lett., 31, L14307, doi:10.1029/2004GL020296, 2004.
Vila-Costa, M., Simó, R., Harada, H., Gasol, J. M., Slezak, D., and Kiene, R. P.: Dimethylsulfoniopropinate uptake by marine phytoplankton, Science, 314, 652, 2006.
Vissher, P. T., Kiene, R. P., and Taylor, B. F.: Demethylation and cleavage of demethylsulfoniopropionate in marine intertidal sediments, FEMS Microbiol. Ecol., 14, 179–190, 1994.
Walter, S., Peeken, I., Lochte, K., and Bange, H. W.: Nitrous oxide measurements during EIFEX, the European Iron Fertilisation Experiment in the subpolar South Atlantic Ocean, Geophys. Res. Lett., 32, L23613, doi:10.1029/2005GL024619, 2005.

BGD
11, 12531–12569, 2014

Wanninkhof, R.: Relationship between wind speed and gas exchange over the ocean, J. Geophys. Res., 97, 7373–7382, 1992.
Weisenburg, D. A. and Guinasso, N. L.: Equilibrium solubilities of methane, carbon monoxide and hydrogen in water and seawater, J. Chem. Eng. Data, 24, 354–360, 1979.
Weller, D. I., Law, C. S., Marriner, A., Nodder, S. D., Chang, F. H., Stephens, J. A., Wilhelm, S. W., Boyd, P. W., Sutton, P. J. H.: Temporal variation of dissolved methane in a subtropical mesoscale eddy during a phytoplankton bloom in the southwest Pacific Ocean, Prog. Oceanogr., 116, 193–206, 2013.
Weiss, R. F. and Prince, B. A.: Nitrous oxide solubility in water and seawater, Mar. Chem., 8, 347–359, 1980.
Wingenter, O. W., Haase, K. B., Strutton, P., Friedrich, G., Meinardi, S., Blake, D. R., and Rowland, F. S.: Changing concentrations of CO, CH_4, C_5H_8, CH_3Bt, CH_3I and dimethyl sulfide during the Southern Ocean Iron Enrichment Experiments, P. Natl. Acad. Sci. USA, 101, 8537–8541, 2004.
Wolfe, R. S.: Microbial formation of methane, Adv. Microb. Physiol., 6, 107–146, 1971.
Wuebbles, D. J. and Hayhoe, K.: Atmospheric methane and global change, Earth-Sci. Rev., 57, 177–210, 2002.
Zhang, Y., Lacan, F., and Jeandel, C.: Dissolved rare earth elements tracing lithogenic inputs over the Kerguelen Plateau (Southern Ocean), Deep-Sea Res. Pt. II, 55, 638, 2008.
Zhou, M., Zhu, Y., d'Ovidio, F., Park, Y.-H., Durand, I., Kestenare, E., Sanial, V., Van-Beek, P., Queguiner, B., Carlotti, F., and Blain, S.: Surface currents and upwelling in Kerguelen Plateau regions, Biogeosciences Discuss., 11, 6845–6876, doi:10.5194/bgd-11-6845-2014, 2014.

BGD
11, 12531–12569, 2014

Table 1. General oceanographic features of the sampled stations during the Keops 2 cruise.

Biogeochemical Provinces	Stations	Latitude °E	Longitude °S	Date mm-dd-yy	Bottom Depth (m)	MLD (m)	Temperature (°C)	Salinity	Oxygen (µmol kg^{-1})
	OISO-6	−44.59	52.06	10-15-11	3260	110	3.68 (3.66–3.68)	33.80 (33.80–33.81)	317.4 (314–318)
	OISO-7	−47-4	58.00	10-16-11	4300	127	4.75 (4.73–4.76)	33.79 (33.8–33.81)	308.4 (305–309)
N–S transect									
	A3-1	−50.38	72.05	10-19-11	535	181	1.68 (1.68–1.73)	33.89 (33.85–33.91)	325.9 (321–327)
	A3-2	−50.38	72.05	10-16-11	527	165	2.16 (2.10–2.18)	33.91 (33.911–33.913)	333.2 (329–335)
	TNS10	−50.12	72.07	10-21-11	565	163	1.67 (1.59–1.68)	33.90 (33.80–33.93)	325.9 (314–327)
Eddy	TNS09	−49.47	72.12	10-21-11	615	137	1.75 (1.66–1.89)	33.91 (33.80–33.84)	321.1 (265–331)
Eddy	TNS08	−49.27	72.14	10-21-11	1030	139	2.11 (2.06–2.12)	33.869 (33.86–33.87)	329.4 (324–328)
	TNS07	−49.08	72.17	10-22-11	1890	62	2.10 (1.95–2.16)	33.86 (33.86–33.87)	327.7 (327–331)
	TNS06	−48.48	71.18	10-22-11	1885	67	2.32 (2.23–2.42)	33.846 (33.84–33.85)	327.6 (315–316)
	TNSO5	−48.28	72.12	10-22-11	2060	114	2.22 (2.09–2.26)	33.85 (33.85–33.86)	326.7 (323–328)
	TNS03	−47.05	71.55	10-23-11	540	111	2.17 (2.06–2.26)	33.89 (33.88–33.89)	307.6 (304–310)
	TNS02	−47.19	71.42	10-23-11	520	65	3.60 (3.38–3.67)	33.69 (33.68–33.69)	318.6 (317–319)
	TNS01	−46.49	71.30	10-23-11	2280	45	4.02 (3.96–4.13)	33.71 (33.71–33.72)	316.1 (315–318)
HNLC	RK2-2	−50.21	66.43	10-23-11	2300	111	2.11 (2.06–2.14)	33.78 (33.77–33.78)	326.7 (326–327)
E–W transect									
(Shelf)	TEW1	−49.08	69.50	10-31-11	86	16	3.27 (3.17–3.36)	33.61 (33.61–33.62)	344.16 (340–345)
(Shelf)	TEW2	−48.53	70.39	10-31-11	84	40	2.55 (2.49–2.68)	33.75 (33.75–33.76)	332.0 (327–337)
(Shelf)	TEW3	−48.47	71.01	10-31-11	565	62	2.17 (2.12–2.31)	33.86 (33.86–33.87)	329.69 (328–331)
(NPF)	TEW4	−48.37	71.28	11-01-11	1585	95	2.54 (2.41–2.60)	33.85 (33.85–33.86)	334.60 (331–337)
	TEW5	−48.28	72.47	11-01-11	2275	60	2.51 (2.39–2.60)	33.84 (33.84–33.85)	331.42 (327–336)
(SPF)	TEW7	−48.27	73.59	11-02-11	2510	17	4.02 (3.91–4.10)	33.78 (33.784–33.79)	315.95 (346–349)
	TEW8	−48.28	75.19	11-02-11	2786	22	4.15 (4.08–4.18)	33.76 (33.76–33.77)	338.75 (347–350)
Time Series Stations									
	E1-1	−48.27	72.11	10-28-11	2056	84	2.48 (2.36–2.54)	33.85 (33.84–33.85)	331.54 (328–333)
	E1-2	−48.31	72.04	11-01-11	2003	42	2.42 (2.28–2.56)	33.85 (33.85–33.86)	331.68 (329–333)
	E1-3	−48.41	71.58	11-03-11	1915	41	2.74 (2.60–2.81)	33.84 (33.84–33.85)	332.08 (331–332)
	E1-4W	−48.45	71.25	11-11-11	1384	67	2.36 (2.07–2.51)	33.90 (33.90–33.91)	329.95 (326–332)
	E1-4E	−48.42	72.33	11-12-11	2210	77	3.15 (2.78–3.19)	33.84 (33.83–33.85)	329.89 (326–331)
	E1-5	−48.24	71.50	11-18-11	1920	36	2.53 (2.50–2.62)	33.85 (33.85–33.85)	326.97 (330–333)

BGD
11, 12531–12569, 2014

Table 2. Inventories of gases and nutrients estimated in the mixed layer (ML) and the entire water column, along with GHG concentrations, wind velocities and concomitant estimated gas exchange across the air–sea interface.

Station	Inventory in the MLD					Inventory in the Water Column				GHGs		Wind	Flux LM86		Flux W92	
	Chl a[a] mg m^{-2}	CH_4 mmol m^{-2}	N_2O mmol m^{-2}	NO_3^- mol m^{-2}	PO_4^{3-} mol m^{-2}	N_2O mmol m^{-2}	CH_4 mmol m^{-2}	NO_3^- mol m^{-2}	PO_4^{3-} mol m^{-2}	N_2O nM	CH_4 nM	m s^{-1}	N_2O µmol m^{-2} d^{-1}	CH_4	N_2O µmol m^{-2} d^{-1}	CH_4
N–S Transect																
A3-1	12.60	3.00	2.43	5.41	0.293	5.72	4.12	7.342	0.940	13.73	6.56	6.58	−1.54	18.75	−2.96	35.93
A3-2	35.48	3.31	1.81	4.38	0.300	5.273	3.31	15.04	1.024	11.64	8.37	11.39	−10.5	14.24	−22.9	29.70
TNS10	14.09	1.39	2.56	4.79	0.319	9.29	2.17	16.03	1.077	15.49	7.79	12.66	3.57	14.90	6.56	27.48
TNS09	35.58	1.33	2.23	3.91	0.254	7.51	1.87	12.53	0.864	15.89	14.54	14.38	5.08	38.10	9.36	70.26
TNS08	23.23	0.68	2.16	3.98	0.260	9.27	1.58	15.75	1.038	15.46	5.65	11.89	4.29	7.80	7.92	14.38
TNS07	25.45	0.25	1.02	1.69	0.111	9.99	1.80	15.74	1.072	16.92	4.01	11.89	8.65	2.03	15.55	3.66
TNS06	16.33	0.57	0.92	1.83	0.123	8.65	2.54	15.93	1.070	13.81	8.74	11.89	−0.78	17.59	−1.20	31.64
TNSO5	17.19	0.74	1.68	3.07	0.212	9.27	2.46	15.39	1.070	14.67	6.41	11.40	1.81	9.91	3.26	17.82
TNS03	17.28	0.88	1.75	3.06	0.214	7.75	3.14	12.46	0.875	11.05	7.23	11.40	4.13	9.93	6.85	16.44
TNS02	11.25	0.26	0.91	1.73	0.123	8.27	1.57	15.08	1.046	13.92	4.38	9.73	1.48	3.03	2.45	5.00
TNS1	11.21	0.39	0.63	1.07	0.076	8.89	3.16	14.17	0.976	13.95	8.48	9.73	2.26	14.40	3.74	23.84
RK2-2	14.89	0.64	1.63	2.79	0.197	2.83	1.06	4.900	0.347	14.83	6.29	6.86	0.89	4.09	1.34	6.15
W–E Transect																
TEW1	9.78	0.19	0.26	3.40	0.412	1.18	1.30	1.560	0.111	15.29	9.50	4.60	0.87	3.15	1.69	6.15
TEW2	9.87	0.43	0.62	0.84	1.073	1.12	1.74	1.873	0.133	15.03	9.88	4.60	0.54	3.24	1.06	6.33
TEW3	8.77	0.73	0.91	0.51	1.566	7.41	2.40	14.97	1.072	15.56	14.09	4.60	0.67	5.25	1.32	10.24
E1-2	15.33	0.52	0.20	0.82	1.167	9.78	2.80	15.24	1.051	14.95	11.42	6.92	1.34	11.67	2.01	17.57
TEW4	35.53	0.40	1.63	0.30	2.468	10.3	1.81	15.74	1.106	16.62	3.50	6.92	3.76	0.21	5.67	0.32
TEW5	23.11	0.38	0.99	0.52	1.619	10.21	2.61	15.62	1.099	16.31	6.35	6.92	3.28	4.34	4.94	6.54
TEW7	75.45	0.19	0.23	2.39	0.353	9.26	7.44	15.23	1.087	12.90	10.87	8.04	−0.96	15.42	−1.52	23.78
TEW8	59.52	0.10	0.37	1.52	0.472	10.05	1.59	15.27	1.058	15.77	4.95	8.04	5.25	3.52	8.10	5.42

[a] Inventories estimated from the photic zone.

BGD
11, 12531–12569, 2014

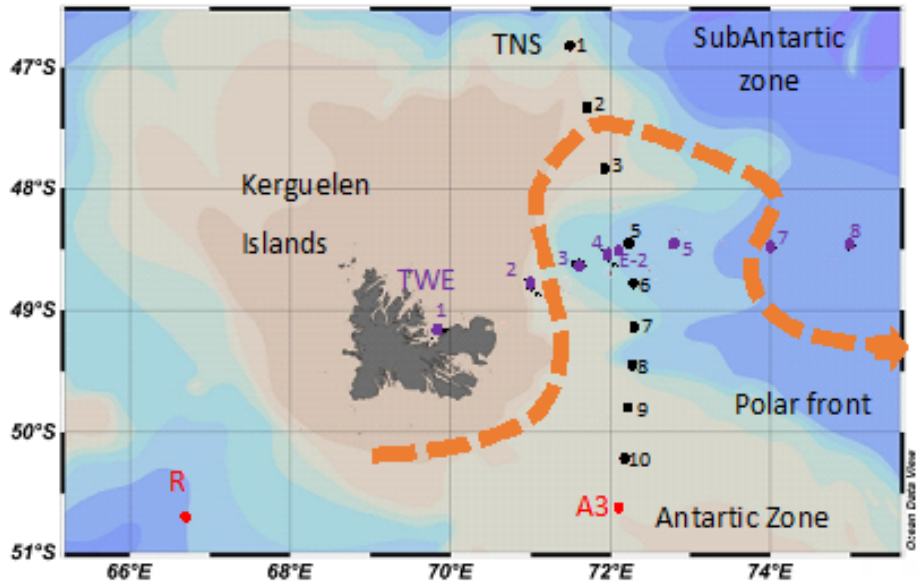

Figure 1. Map showing the location of biogeochemical stations sampled during the Keops 2 cruise. Bathymetric topography is shown in the main oceanographic region. The orange line delimits the position of the polar front. The sampled transects are indicated.

BGD
11, 12531–12569, 2014

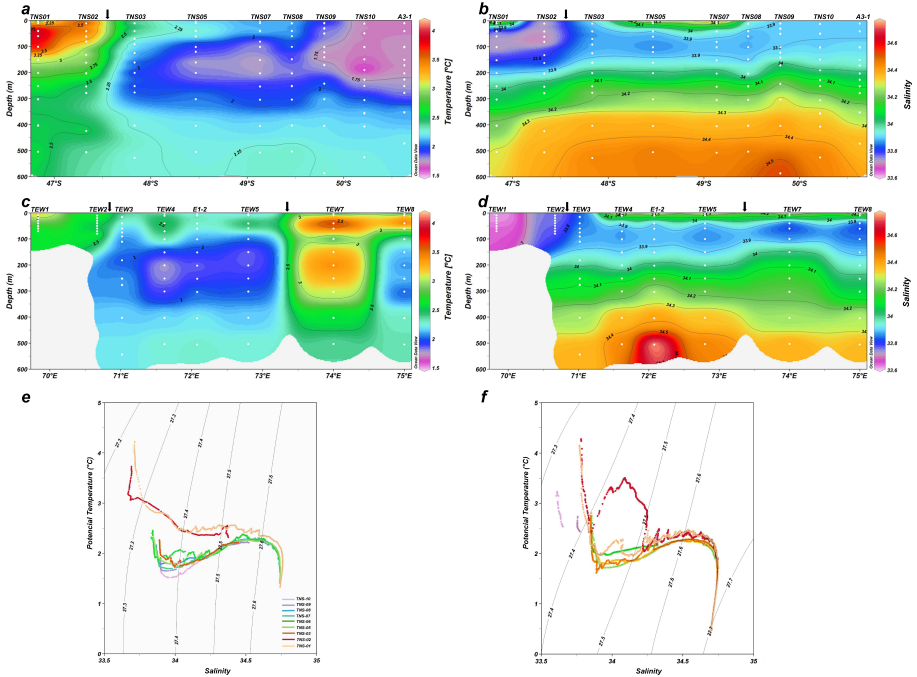

Figure 2. Salinity, temperature and T-S diagrams in **(a)** N–S transect; and **(b)** W–E transect, highlighting the water mass characteristics north (green) and south (red) of the polar front. In addition, a third station (purple) is shown, indicating the complexity of the PFZ as a region of enhanced water mass mixing.

BGD
11, 12531–12569, 2014

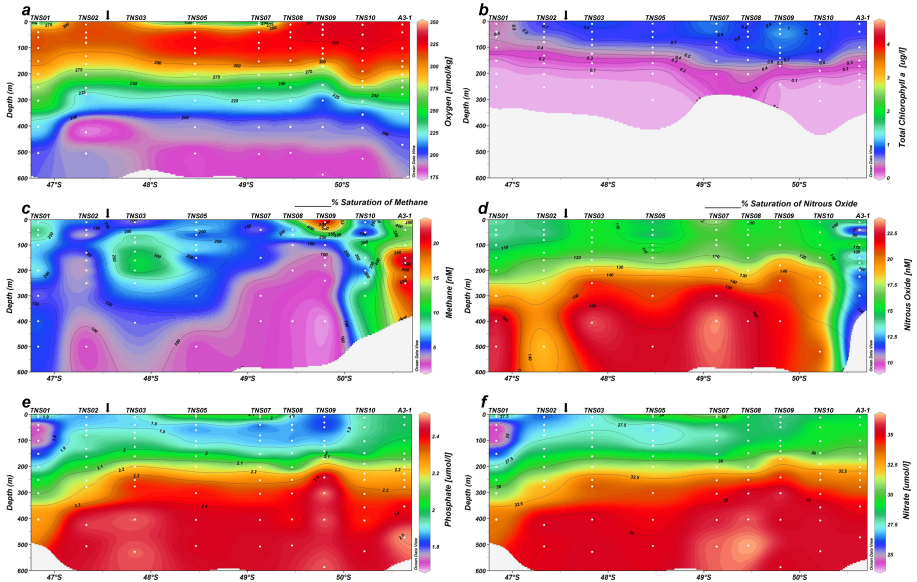

Figure 3. Vertical cross section of **(a)** dissolved oxygen ($\mu mol\,L^{-1}$) **(b)** chlorophyll *a* ($\mu g\,L^{-1}$) **(c)** methane ($nmol\,L^{-1}$), **(d)** nitrous oxide ($nmol\,L^{-1}$), **(e)** phosphate ($\mu mol\,L^{-1}$) and **(f)** nitrate ($\mu mol\,L^{-1}$) along the zonal transect between 69–75° E.

BGD
11, 12531–12569, 2014

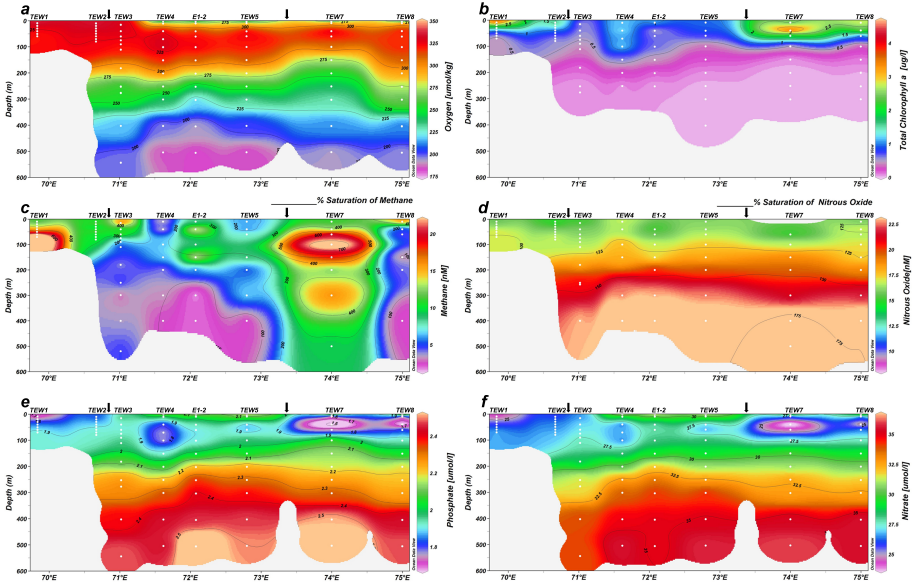

Figure 4. Vertical cross section of **(a)** dissolved oxygen ($\mu mol\,L^{-1}$), **(b)** chlorophyll *a* ($\mu g\,L^{-1}$), **(c)** methane ($nmol\,L^{-1}$), **(d)** nitrous oxide ($nmol\,L^{-1}$), **(e)** phosphate ($\mu mol\,L^{-1}$) and **(f)** nitrate ($\mu mol\,L^{-1}$) along the meridional transect between 45–51° S.

BGD
11, 12531–12569, 2014

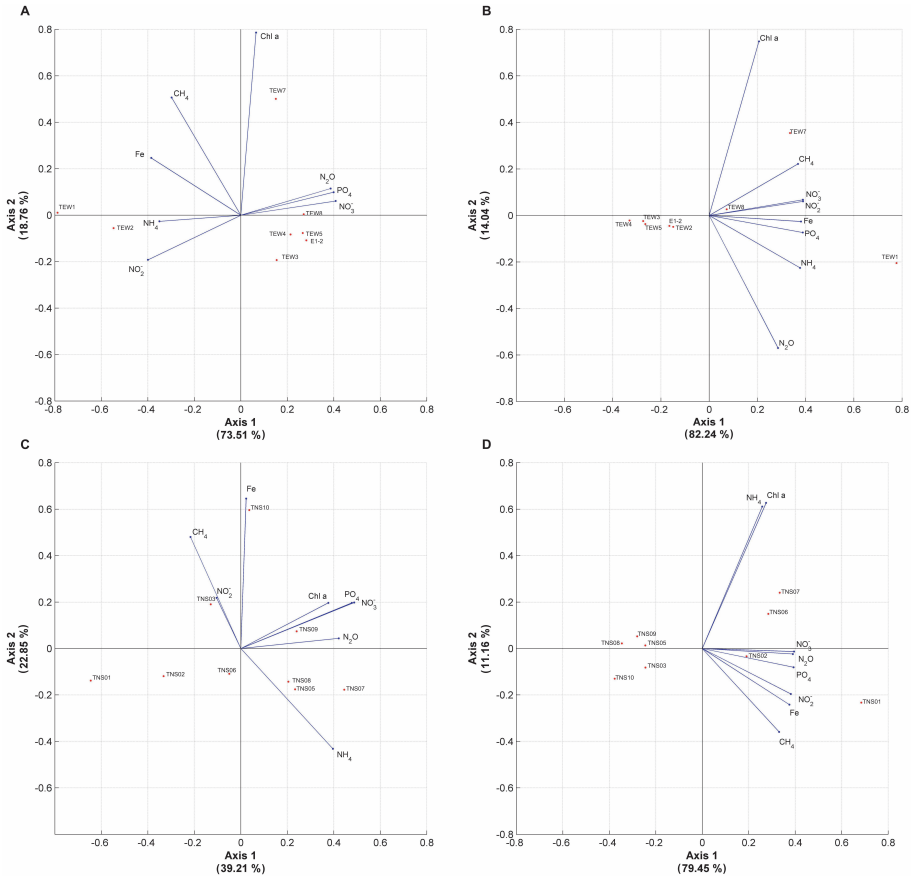

Figure 5. PCA analysis with data from the surface to a depth of 500 m and from the surface to the ML's base. Each station along with the eigenvectors are included.

BGD
11, 12531–12569, 2014

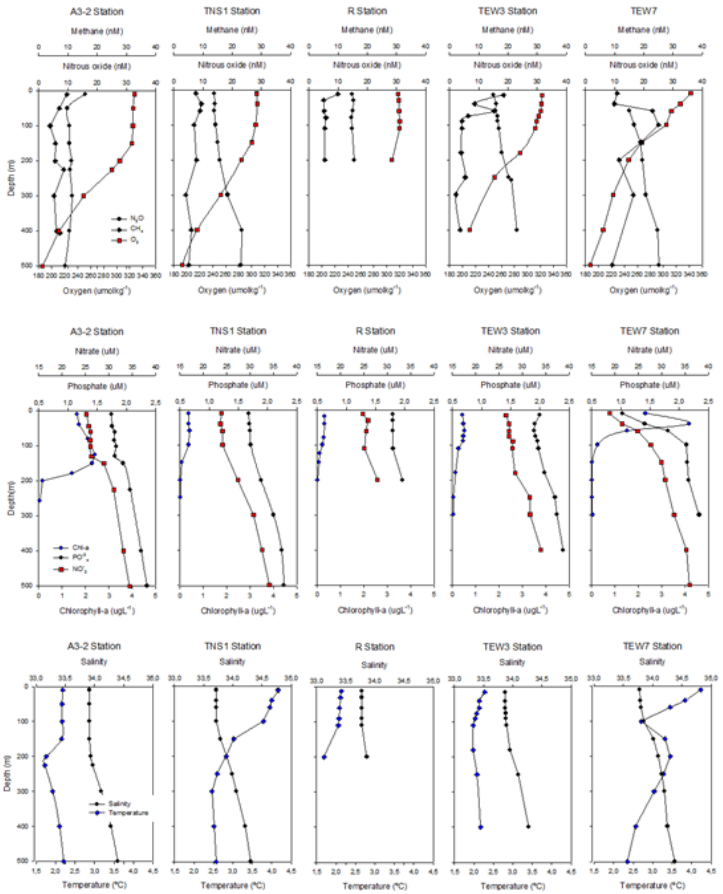

Figure 6. Vertical distribution of biogeochemical variables from selected stations with particular oceanographic and biogeochemical characteristics. Different biogeochemical regimes are defined as HNLC area (St R), northern and southern area of Polar front (St. NS01 and A3) and within the Polar front (Sts. TWE03 and TWE07).

BGD
11, 12531–12569, 2014